Author(s): Kukkola, Jarno & Hinkkanen, Marko

Title: State observer for sensorless control of a grid-connected converter equipped with an LCL filter: Direct discrete-time design

Year: 2015

Version: Post print

Please cite the original version:

Kukkola, Jarno & Hinkkanen, Marko. 2015. State observer for sensorless control of a grid-connected converter equipped with an LCL filter: Direct discrete-time design. IEEE Energy Conversion Congress and Exposition (ECCE). 8. ISBN 978-1-4673-7150-6 (electronic). DOI: 10.1109/ecce.2015.7310435.

State Observer for Sensorless Control of a Grid-Connected Converter Equipped With an LCL Filter: Direct Discrete-Time Design

Jarno Kukkola and Marko Hinkkanen
Aalto University, Department of Electrical Engineering and Automation
P.O. Box 13000, FI-00076 Aalto, Espoo, Finland

***Abstract*—Synchronization with the power system is an essential part of control of grid-connected converters. This paper proposes a grid-voltage sensorless synchronization and control scheme for a grid-connected converter equipped with an LCL filter, measuring only the converter currents and the DC voltage. A discrete-time pole-placement design method is used to formulate an adaptive full-order observer for estimation of the angle and magnitude of the grid voltage. The analytically derived design is experimentally validated, and the results demonstrate rapid convergence of the estimated angle and magnitude.**

***Index Terms*—Active front-end rectifier, adaptive observer, distributed generation, line-voltage sensorless, small-signal linearization, state feedback, synchronization**

I. Introduction

Grid-connected converters are increasingly used to connect various renewable energy sources to the electric power system. A growing trend is to replace a conventional inductive L filter (between the converter and the grid) with an LCL filter in order to fulfill the current harmonic limits presented in the standards, e.g., [1]. A factor behind this trend is higher switching harmonics attenuation provided by the LCL filter, which enables a physically smaller and cheaper filter at low switching frequencies, e.g., $4 \ldots 8$ kHz [2].

The converter equipped with an LCL filter is also an attractive solution for low-harmonic active front-end rectifiers of variable-speed motor drives, where regenerative braking, adjustable DC-link voltage, and adjustable power factor enable energy flow optimization. In drives, operation without position or speed sensors provides cost savings and increases reliability [3]. Overall costs of a drive with an active front-end rectifier can be further reduced by replacing the grid voltage sensors with estimation and implementing active damping of the LCL-filter resonance without extra sensors as in [4].

Synchronization with the grid is needed in order to control instantaneous active and reactive power injected by the converter. However, only a few grid-voltage sensorless synchronization methods have been presented in the case of the LCL filter [4]–[11]. Sensorless synchronization has been obtained using the instantaneous power theory [4] and virtual flux models [5], [6]. Alternatively, the grid voltage can be estimated using observers [7]–[13]. Solutions relying on the Kalman filter have been proposed [7]–[9]. Although the Kalman filter can be described as a statistically optimal estimator, its drawback is that the process noise parameters are needed for tuning of the observer. These noise parameters are often determined by trial and error [7].

A subcategory of the observers is model-reference adaptive observers, which are able to adjust internal model parameters in real time. Adaptive observers have been used for estimation of the rotor speed, position, and flux magnitude in motor drives, e.g., in [14], and, correspondingly, for estimation of the grid-voltage frequency, angle, and magnitude in grid-connected converters [8], [10]–[13]. The estimation error of the converter current includes the information of the grid-voltage angle and amplitude [11], [12].

Control of a converter is typically implemented on a microprocessor and the sampling of the converter current is synchronized with the pulse-width modulation (PWM). Frequently, the control algorithms are designed in the continuous-time domain and then discretized. This principle works well in many cases. However, when the LCL-filter resonance is relatively close to the switching frequency, only a few samples are obtained within the period of the resonance frequency. Then, the direct discrete-time design is preferable, e.g., in the case of current control [15]. For sensorless control of a converter equipped with the LCL filter, a continuous-time design has been presented for a model-based full-order observer in [11]. However, no analytical direct discrete-time design method has been presented for the adaptive full-order observer in this application.

Main contributions of this paper are: 1) A direct discrete-time design method is proposed for an adaptive full-order observer enabling grid-voltage sensorless control of a grid-connected converter equipped with an LCL filter; 2) Estimation error dynamics of the observer are analyzed by means of small-signal linearization; 3) The analytically derived design is experimentally verified. Furthermore, the proposed observer is compared with the observer designed in the continuous-time domain [11]. The presented design method retains analytical connection between the physical model parameters of the LCL filter and the observer dynamics. This connection generalizes the method for different parameter sets and enables automatic tuning if the model parameters are known or estimated.

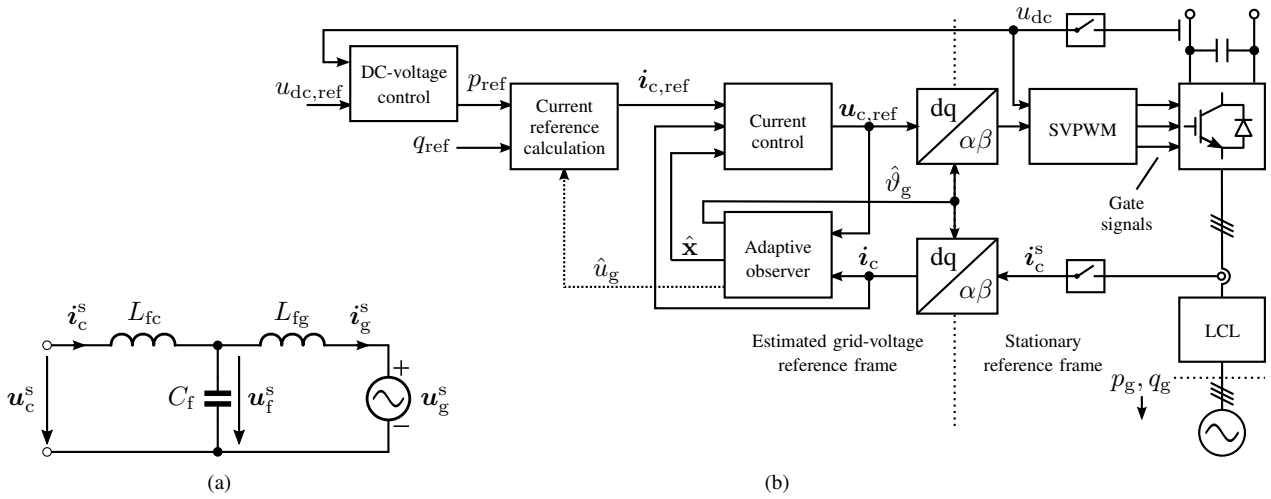

Fig. 1. (a) Space-vector circuit model of the grid-connected LCL filter in stationary coordinates (marked with the superscript s). (b) Grid-voltage sensorless control system. The angle $\omega_{\mathrm{g}} T_{\mathrm{s}}$ caused by the computational delay is compensated for in the dq $\rightarrow \alpha\beta$ transformation (not explicitly shown in the figure).

II. System Model

Switching-cycle-averaged complex-valued space vectors are used. Complex-valued, matrix, and vector quantities are marked with boldface symbols. The equivalent circuit model of the LCL filter is presented in Fig. 1(a). The grid-voltage vector in the stationary reference frame (marked with the superscript s) is

$$\boldsymbol{u}_{\mathrm{g}}^{\mathrm{s}} = \mathrm{e}^{\mathrm{j}\vartheta_{\mathrm{g}}} u_{\mathrm{g}}, \tag{1}$$

where $\vartheta_{\mathrm{g}} = \int \omega_{\mathrm{g}} \mathrm{d}t$ is the angle, ω_{g} is the angular frequency, and u_{g} is the amplitude.

In synchronous grid-voltage oriented coordinates (marked with the superscript g), the dynamics of the converter current $\boldsymbol{i}_{\mathrm{c}}^{\mathrm{g}}$ are

$$\begin{aligned} \frac{\mathrm{d}\mathbf{x}^{\mathrm{g}}}{\mathrm{d}t} &= \begin{bmatrix} -\mathrm{j}\omega_{\mathrm{g}} & -\frac{1}{L_{\mathrm{fc}}} & 0 \\ \frac{1}{C_{\mathrm{f}}} & -\mathrm{j}\omega_{\mathrm{g}} & -\frac{1}{C_{\mathrm{f}}} \\ 0 & \frac{1}{L_{\mathrm{fg}}} & -\mathrm{j}\omega_{\mathrm{g}} \end{bmatrix} \mathbf{x}^{\mathrm{g}} + \begin{bmatrix} \frac{1}{L_{\mathrm{fc}}} \\ 0 \\ 0 \end{bmatrix} \boldsymbol{u}_{\mathrm{c}}^{\mathrm{g}} - \begin{bmatrix} 0 \\ 0 \\ \frac{1}{L_{\mathrm{fg}}} \end{bmatrix} u_{\mathrm{g}} \\ \boldsymbol{i}_{\mathrm{c}}^{\mathrm{g}} &= \underbrace{\begin{bmatrix} 1 & 0 & 0 \end{bmatrix}}_{\mathbf{C}_{\mathrm{c}}} \mathbf{x}^{\mathrm{g}} \end{aligned} \tag{2}$$

where the state vector is $\mathbf{x}^{\mathrm{g}} = [\boldsymbol{i}_{\mathrm{c}}^{\mathrm{g}}, \boldsymbol{u}_{\mathrm{f}}^{\mathrm{g}}, \boldsymbol{i}_{\mathrm{g}}^{\mathrm{g}}]^{\mathrm{T}}$, the voltage across the filter capacitor C_{f} is $\boldsymbol{u}_{\mathrm{f}}^{\mathrm{g}}$, and the converter and grid currents are $\boldsymbol{i}_{\mathrm{c}}^{\mathrm{g}}$ and $\boldsymbol{i}_{\mathrm{g}}^{\mathrm{g}}$, respectively. The resonance frequency of the LCL filter is

$$\omega_{\mathrm{p}} = \sqrt{(L_{\mathrm{fc}} + L_{\mathrm{fg}})/(L_{\mathrm{fc}} L_{\mathrm{fg}} C_{\mathrm{f}})}. \tag{3}$$

The losses of the filter are neglected, which represents the worst-case situation for the resonance of the LCL filter.

A zero-order hold for the switching-cycle-averaged converter output voltage is assumed and synchronous sampling is used. In addition, the amplitude u_{g} and frequency ω_{g} of the grid voltage are assumed to vary slowly, i.e., to be constant during the sampling period T_{s}. Under these assumptions, the discrete-time model of (2) is [15]

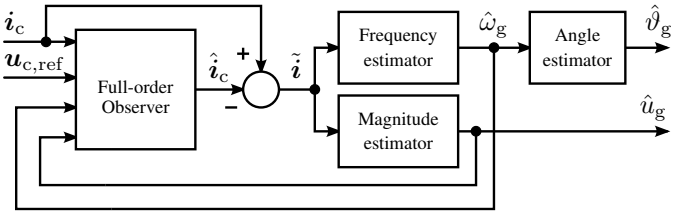

Fig. 2. Internal structure of the adaptive observer.

$$\begin{aligned} \mathbf{x}^{\mathrm{g}}(k+1) &= \boldsymbol{\Phi} \mathbf{x}^{\mathrm{g}}(k) + \boldsymbol{\Gamma}_{\mathrm{c}} \boldsymbol{u}_{\mathrm{c}}^{\mathrm{g}}(k) + \boldsymbol{\Gamma}_{\mathrm{g}} u_{\mathrm{g}}(k) \\ \boldsymbol{i}_{\mathrm{c}}^{\mathrm{g}}(k) &= \mathbf{C}_{\mathrm{c}} \mathbf{x}^{\mathrm{g}}(k) \end{aligned} \tag{4}$$

Furthermore, the closed-form expressions for the elements of the state-transition matrix $\boldsymbol{\Phi}$ and the input vectors $\boldsymbol{\Gamma}_{\mathrm{c}}$ and $\boldsymbol{\Gamma}_{\mathrm{g}}$ are given in Appendix A as functions of the LCL-filter parameters. The grid-voltage angle is

$$\vartheta_{\mathrm{g}}(k+1) = \vartheta_{\mathrm{g}}(k) + T_{\mathrm{s}} \omega_{\mathrm{g}} \tag{5}$$

in the discrete-time domain.

III. Adaptive Full-Order Observer

The control structure is illustrated in Fig. 1(b). Control of the converter is implemented in the estimated grid-voltage reference frame that is aligned with the estimated grid-voltage vector. Synchronization is obtained using an adaptive observer. The structure of the adaptive observer is shown in Fig. 2. The angular frequency $\hat{\omega}_{\mathrm{g}}$, the angle $\hat{\vartheta}_{\mathrm{g}}$, and the magnitude $\hat{u}_{\mathrm{g}}$ of the grid voltage are estimated in the outer loops, while the state vector $\hat{\mathbf{x}}$ is estimated by the full-order state observer. The full-order observer is

$$\begin{aligned} \hat{\mathbf{x}}(k+1) &= \hat{\boldsymbol{\Phi}} \hat{\mathbf{x}}(k) + \hat{\boldsymbol{\Gamma}}_{\mathrm{c}} \boldsymbol{u}_{\mathrm{c}}(k) + \hat{\boldsymbol{\Gamma}}_{\mathrm{g}} \hat{u}_{\mathrm{g}}(k) \\ &\quad + \mathbf{K}_{\mathrm{o}} [\boldsymbol{i}_{\mathrm{c}}(k) - \hat{\boldsymbol{i}}_{\mathrm{c}}(k)] \\ \hat{\boldsymbol{i}}_{\mathrm{c}}(k) &= \mathbf{C}_{\mathrm{c}} \hat{\mathbf{x}}(k) \end{aligned} \tag{6}$$

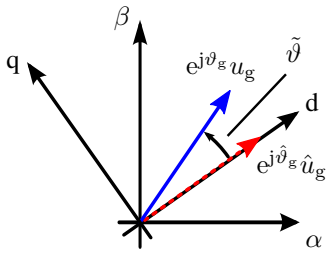

Fig. 3. Orientation of the estimated grid-voltage reference frame.

where $\boldsymbol{u}_c(k) = \boldsymbol{u}_{c,ref}(k-1)$ is obtained from the delayed converter-voltage reference, $\mathbf{K}_o = [\boldsymbol{k}_{o1}\ \boldsymbol{k}_{o2}\ \boldsymbol{k}_{o3}]^T$ is the observer gain vector, and $\hat{\mathbf{\Phi}}$, $\hat{\mathbf{\Gamma}}_c$, and $\hat{\mathbf{\Gamma}}_g$ are adaptive model matrices that are obtained replacing the actual angular frequency ω_g with the estimated angular frequency $\hat{\omega}_g$ in the matrices. According to (5), a natural estimator for the angle is

$$\hat{\vartheta}_g(k+1) = \hat{\vartheta}_g(k) + T_s\hat{\omega}_g(k) \tag{7}$$

A. Estimation-Error Dynamics

There can be angle displacement between the actual and estimated grid-voltage vector (cf. Fig. 3). From (5) and (7), the dynamics of the angle error $\tilde{\vartheta} = \vartheta_g - \hat{\vartheta}_g$ become

$$\tilde{\vartheta}(k+1) = \tilde{\vartheta}(k) + T_s\tilde{\omega}_g(k) \tag{8}$$

where $\tilde{\omega}_g = \omega_g - \hat{\omega}_g$ is the frequency estimation error. Since the system model and the control algorithm are in the different coordinates, the discrete-time model (4) is transformed into the estimated grid-voltage reference frame applying:

$$\begin{aligned}\mathbf{x}^g(k+1) &= e^{-j\tilde{\vartheta}(k+1)}\mathbf{x}(k+1)\\ \mathbf{x}^g(k) &= e^{-j\tilde{\vartheta}(k)}\mathbf{x}(k)\\ \boldsymbol{u}_c^g(k) &= e^{-j\tilde{\vartheta}(k)}\boldsymbol{u}_c(k)\end{aligned} \tag{9}$$

Together with (8), the resulting dynamics are

$$\begin{aligned}\mathbf{x}(k+1) &= e^{jT_s\tilde{\omega}_g(k)}\mathbf{\Phi}\mathbf{x}(k) + e^{jT_s\tilde{\omega}_g(k)}\mathbf{\Gamma}_c\boldsymbol{u}_c(k)\\ &\quad + e^{j\tilde{\vartheta}(k+1)}\mathbf{\Gamma}_g u_g(k)\\ \boldsymbol{i}_c(k) &= \mathbf{C}_c\mathbf{x}(k)\end{aligned} \tag{10}$$

From (6), (8), and (10), the dynamics of the estimation-error $\mathbf{e}(k) = \mathbf{x}(k) - \hat{\mathbf{x}}(k)$ become

$$\begin{aligned}\mathbf{e}(k+1) &= (\hat{\mathbf{\Phi}} - \mathbf{K}_o\mathbf{C}_c)\mathbf{e}(k) + \left(e^{jT_s\tilde{\omega}_g(k)}\mathbf{\Phi} - \hat{\mathbf{\Phi}}\right)\mathbf{x}(k)\\ &\quad + \hat{\mathbf{\Gamma}}_g\tilde{u}_g(k) + \left(e^{jT_s\tilde{\omega}_g(k)}\mathbf{\Gamma}_c - \hat{\mathbf{\Gamma}}_c\right)\boldsymbol{u}_c(k)\\ &\quad + \left(e^{j[\tilde{\vartheta}(k)+T_s\tilde{\omega}_g(k)]}\mathbf{\Gamma}_g - \hat{\mathbf{\Gamma}}_g\right)u_g(k)\end{aligned} \tag{11}$$

where $\tilde{u}_g = u_g - \hat{u}_g$ is the estimation error of the grid voltage. As can be seen, (11) is nonlinear with respect to the angle error $\tilde{\vartheta}$ and the angular-frequency error $\tilde{\omega}_g$. Furthermore, the matrices $\hat{\mathbf{\Phi}}(\hat{\omega}_g)$, $\hat{\mathbf{\Gamma}}_c(\hat{\omega}_g)$, and $\hat{\mathbf{\Gamma}}_g(\hat{\omega}_g)$ depend on the estimated angular frequency $\hat{\omega}_g$ and moreover on the estimation error $\tilde{\omega}_g$.

B. Small-Signal Linearization

The nonlinear dynamics are analyzed in an operating point. Operating-point quantities are marked with the subscript 0. If the accurate model parameters are assumed and the gain $\mathbf{K}_o$ is selected such that the eigenvalues of $\mathbf{\Phi} - \mathbf{K}_o\mathbf{C}_c$ are inside the unit circle, the system has an equilibrium point $\{\mathbf{e}_0 = 0,\ \tilde{u}_0 = 0,\ \tilde{\omega}_0 = 0,\ \tilde{\vartheta}_0 = 0\}$, where the estimation error is zero in steady state. In the vicinity of the equilibrium point, the system (11) has linearized dynamics

$$\begin{aligned}\mathbf{e}(k+1) &= (\mathbf{\Phi} - \mathbf{K}_o\mathbf{C}_c)\,\mathbf{e}(k) + j\mathbf{\Gamma}_g u_{g0}\tilde{\vartheta}(k)\\ &\quad + \underbrace{\left[j\mathbf{\Gamma}_g T_s - \left(\frac{d\hat{\mathbf{\Gamma}}_g}{d\tilde{\omega}}\right)_0\right]u_{g0}}_{\mathbf{\Gamma}_\omega}\tilde{\omega}(k) + \mathbf{\Gamma}_g\tilde{u}_g(k).\end{aligned} \tag{12}$$

The linearized dynamics are derived in Appendix B.

The converter current is the only measured state variable. Thus, it is interesting to analyze the dynamics of the estimation error $\tilde{\boldsymbol{i}} = \mathbf{C}_c\mathbf{e}$ of the converter current induced by the magnitude and angle deviations, $\tilde{u}_g$ and $\tilde{\vartheta}$, respectively. From (12), the pulse-transfer function from the voltage deviation to the converter-current estimation error is

$$\boldsymbol{G}_{iu}(z) = \frac{\tilde{\boldsymbol{i}}(z)}{\tilde{u}_g(z)} = \frac{\boldsymbol{b}(z)}{\boldsymbol{a}(z)} = \mathbf{C}_c(z\mathbf{I} - \mathbf{\Phi} + \mathbf{K}_o\mathbf{C}_c)^{-1}\mathbf{\Gamma}_g. \tag{13}$$

where

$$\boldsymbol{a}(z) = \det(z\mathbf{I} - \mathbf{\Phi} + \mathbf{K}_o\mathbf{C}_c) \tag{14}$$

and $\boldsymbol{b}(z)$ is the numerator of the transfer function. The coefficient $\mathbf{\Gamma}_\omega$ of the angular frequency error in (12) is minor in comparison with the other coefficients and

$$\lim_{T_s\to 0}\mathbf{\Gamma}_\omega = 0 \tag{15}$$

Therefore, the dynamics can be simplified by approximating $\mathbf{\Gamma}_\omega \approx 0$, and the pulse-transfer function from the angle deviation to the converter current estimation error becomes

$$\boldsymbol{G}_{i\vartheta}(z) = \frac{\tilde{\boldsymbol{i}}(z)}{\tilde{\vartheta}(z)} = \frac{ju_{g0}\cdot\boldsymbol{b}(z)}{\boldsymbol{a}(z)} \tag{16}$$

It can be seen that the estimation-error components in $\tilde{\boldsymbol{i}}$ caused by the voltage and angle deviations are orthogonal, i.e., $\boldsymbol{G}_{i\vartheta} = ju_{g0}\boldsymbol{G}_{iu}$. This forms the basis for the design of the adaptation loops in Sections III-D and III-E.

C. Pole Placement of the Full-Order Observer

Let the desired characteristic polynomial (14) of the estimation-error dynamics be

$$\boldsymbol{a}(z) = (z - \alpha_{o1})(z - \boldsymbol{\alpha}_{o2})(z - \boldsymbol{\alpha}_{o3}). \tag{17}$$

The discrete-time poles α_{o1}, $\boldsymbol{\alpha}_{o2}$, and $\boldsymbol{\alpha}_{o3}$ are mapped via the continuous-time counterpart $(s + \alpha_{od})(s^2 + 2\zeta_{or}\omega_{or}s + \omega_{or}^2)$:

$$\begin{aligned}\alpha_{o1} &= \exp(-\alpha_{od}T_s)\\ \boldsymbol{\alpha}_{o2,3} &= \exp[(-\zeta_{or} \pm j\sqrt{1-\zeta_{or}^2})\omega_{or}T_s]\end{aligned} \tag{18}$$

Continuous-time pole locations are the tuning parameters of the full-order observer. The first-order pole α_{od} is set to

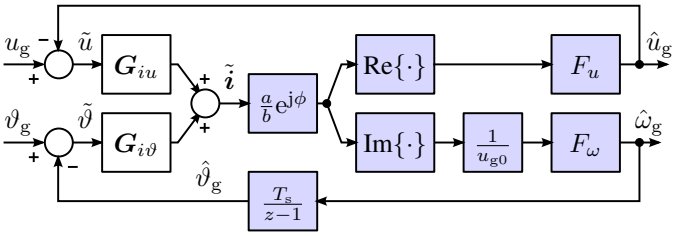

Fig. 4. Small-signal linearized adaptation loops. The blue blocks represent the adaptation laws, i.e., the estimators. For simplicity, the current error component caused by the angular-frequency error $\tilde{\omega}$ is omitted in the figure, since its coefficient is minor in (12).

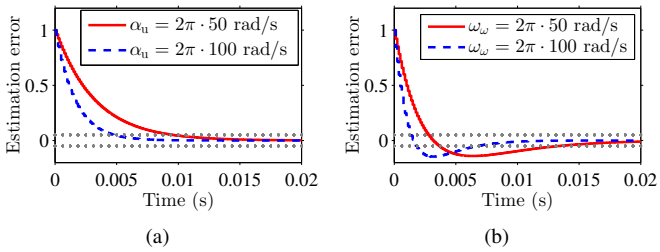

Fig. 5. Estimation-error responses: (a) $\tilde{u}(t)/\Delta u_g$ when a step change Δu_g is applied in the grid-voltage magnitude u_g at $t = 0$ in (23); (b) $\tilde{\vartheta}(t)/\Delta\vartheta_g$ when a step change $\Delta\vartheta_g$ is applied in the angle ϑ_g at $t = 0$ in (25). The tuning parameters of the adaptation loops are: $\alpha_u = \omega_\omega = 2\pi \cdot 50$ rad/s and $\zeta_\omega = 1$ (solid lines) and $\alpha_u = \omega_\omega = 2\pi \cdot 100$ rad/s and $\zeta_\omega = 1$ (dashed lines). The 5-% settling limits are marked with dotted lines.

determine the dominant dynamics of the estimation error and the pair of poles, determined by ω_{or} and ζ_{or}, is placed at a higher frequency. Analytical expressions for calculating the observer gain $\mathbf{K}_o$ have been derived in [15] as a function of the tuning and system (LCL filter) parameters. Furthermore, the selection of the pole locations has been discussed in [15].

D. Quasi-Steady-State Analysis

In order to design adaptation laws for the angle and amplitude estimation of the grid voltage, the estimation error dynamics of the full-order observer in (12) are considered to be much faster than the adaptation mechanisms. From adaptation point of view, it is reasonable to approximate the full-order observer dynamics using quasi-steady-state gains. These gains are obtained for $\tilde{u}_g$ and $\tilde{\vartheta}$ in (13) and (16), respectively, by making $z = 1$. It follows that

$$\tilde{\boldsymbol{i}} = \underbrace{e^{-j\phi}(b/a)}_{\boldsymbol{G}_{iu}(1)}\tilde{u}_g + \underbrace{ju_{g0}e^{-j\phi}(b/a)}_{\boldsymbol{G}_{i\vartheta}(1)}\tilde{\vartheta} \tag{19}$$

where the constants a, b, and ϕ are

$$\begin{aligned}\phi &= (3/2)\omega_g T_s\\ a &= \omega_g C_f L_{fc} L_{fg}(\omega_g^2 - \omega_p^2)(1-\alpha_{o1})(1-\boldsymbol{\alpha}_{o2})(1-\boldsymbol{\alpha}_{o3})\\ b &= 4\sin(\omega_g T_s/2)[\cos(\omega_g T_s) - \cos(\omega_p T_s)]\end{aligned} \tag{20}$$

and ω_p is the resonance frequency (3).

E. Adaptation Laws

As revealed in (19), the real part of the estimation error $\tilde{\boldsymbol{i}}$ of the converter current is strongly affected by the voltage difference $\tilde{u}_g$. On the other hand, the imaginary part of $\tilde{\boldsymbol{i}}$ is strongly affected by the angle difference $\tilde{\vartheta}$. Moreover, if the current-estimation error $\tilde{\boldsymbol{i}}$ is rotated and scaled as $\tilde{\boldsymbol{i}}' = (a/b)e^{j\phi}\tilde{\boldsymbol{i}}$, the real and imaginary parts of the modified error $\tilde{\boldsymbol{i}}'$ can be directly separated into the grid-voltage magnitude and angle estimation, respectively.

Let the grid-voltage estimator be

$$\hat{u}_g(z) = \underbrace{\frac{k_{i,u}}{z-1}}_{F_u(z)}\mathrm{Re}\left\{\frac{a}{b}e^{j\phi}\tilde{\boldsymbol{i}}(z)\right\} \tag{21}$$

and the estimator for the angular frequency be

$$\hat{\omega}_g(z) = \frac{1}{u_{g0}}\underbrace{\left(k_{p,\omega} + \frac{k_{i,\omega}}{z-1}\right)}_{F_\omega(z)}\mathrm{Im}\left\{\frac{a}{b}e^{j\phi}\tilde{\boldsymbol{i}}(z)\right\} \tag{22}$$

Furthermore, the estimator for the grid-voltage angle is given in (7). Fig. 4 shows the linearized adaptation loops, when the proposed adaptation laws are used. Considering the quasi-steady-state relationships $\boldsymbol{G}_{iu}(1)$ and $\boldsymbol{G}_{i\vartheta}(1)$ according to (19), two separate feedback loops are obtained. The closed-loop transfer function of the linearized grid-voltage magnitude adaptation loop becomes

$$G_u(z) = \frac{\hat{u}_g(z)}{u_g(z)} = \frac{F_u(z)}{1+F_u(z)} = \frac{k_{i,u}}{z + k_{i,u} - 1} \tag{23}$$

If the gain is

$$k_{i,u} = 1 - \exp(-\alpha_u T_s) \tag{24}$$

the closed-loop transfer function $G_u(z)$ represents the first-order system with the bandwidth of α_u. This bandwidth is the only parameter needed for tuning of the grid-voltage-magnitude estimation loop. Fig. 5(a) illustrates the estimation error of the voltage when the step change Δu_g is applied in u_g and the selections for the parameters are $\alpha_u = 2\pi \cdot 50$ rad/s and $\alpha_u = 2\pi \cdot 100$ rad/s. The estimation error is less than 5% after $t_{5\%} \approx 3/\alpha_u$. Moreover, the error is practically zero even for the lower α_u after a period of the grid voltage (20 ms).

The closed-loop transfer function of the linearized angle adaptation loop becomes

$$\begin{aligned}G_\vartheta(z) &= \frac{\hat{\vartheta}_g(z)}{\vartheta_g(z)} = \frac{F_\omega(z)\frac{T_s}{z-1}}{1 + F_\omega(z)\frac{T_s}{z-1}}\\ &= \frac{T_s(k_{p,\omega}z + k_{i,\omega} - k_{p,\omega})}{z^2 + (k_{p,\omega}T_s - 2)z + k_{i,\omega}T_s - k_{p,\omega}T_s + 1}\end{aligned} \tag{25}$$

Selecting the gains

$$\begin{aligned}k_{p,\omega} &= [2 - 2\cdot\exp(-\zeta_\omega\omega_\omega T_s)\cos(\sqrt{1-\zeta_\omega^2}\omega_\omega T_s)]/T_s\\ k_{i,\omega} &= [\exp(-2\zeta_\omega\omega_\omega T_s) - 1]/T_s + k_{p,\omega}\end{aligned} \tag{26}$$

the poles of the angle-estimation loop have the natural frequency of ω_ω with the damping ratio of ζ_ω. The angle

estimator is tuned via these parameters. The zero of the pulse-transfer function $G_\vartheta(z)$ introduces overshoot, e.g., in the case of step responses. Thus, it is beneficial to select a high damping ratio, e.g., $\zeta_\omega = 1$. The natural frequency ω_ω is directly related to the convergence speed of the angle tracking. For a step change in the angle, the estimation error is reduced below $\pm 5\%$ in $t_{5\%} \approx 4.2/\omega_\omega$, if $\zeta_\omega = 1$. Fig. 5(b) illustrates the response of the estimation error when the step change $\Delta\vartheta_\mathrm{g}$ is applied in ϑ_g and the parameters are $\omega_\omega = 2\pi \cdot 50$ rad/s and $\omega_\omega = 2\pi \cdot 100$ rad/s. As the figure shows, the estimation error is practically zero after a grid-voltage period (20 ms) even for the smaller ω_ω.

F. Small-Signal Stability

Tuning of the grid-voltage amplitude and angle estimators was based on the quasi-steady-state analysis, and the frequency-error-dependent part $\boldsymbol{\Gamma}_\omega$ of (12) was neglected. However, when the tuning parameters α_u and ω_ω (approximate bandwidths) approach the tuning parameters $\alpha_{\mathrm{o}1}$ and ω_or of the full-order observer, the quasi-steady-state assumption is not valid and the stability of the adaptive observer can be lost. In the following, the stability of the estimation scheme is further analyzed.

Considering (8), (12), (21), and (22), the small-signal model for the closed-loop system is obtained and the estimation-error dynamics are[1]

$$\begin{cases} \mathbf{e}(k+1) = (\boldsymbol{\Phi} - \mathbf{K}_\mathrm{o}\mathbf{C}_\mathrm{c})\,\mathbf{e}(k) + \mathrm{j}\boldsymbol{\Gamma}_\mathrm{g} u_{\mathrm{g}0}\tilde{\vartheta}(k) \\ \qquad\qquad + \boldsymbol{\Gamma}_\omega\tilde{\omega}(k) + \boldsymbol{\Gamma}_\mathrm{g}\tilde{u}_\mathrm{g}(k) \\ \tilde{u}_\mathrm{g}(k+1) = \tilde{u}_\mathrm{g}(k) - k_{\mathrm{i,u}}\,\mathrm{Re}\left\{\dfrac{a}{b}\mathrm{e}^{\mathrm{j}\phi}\mathbf{C}_\mathrm{c}\mathbf{e}(k)\right\} \\ x_\omega(k+1) = x_\omega(k) + \dfrac{1}{u_{\mathrm{g}0}}\,\mathrm{Im}\left\{\dfrac{a}{b}\mathrm{e}^{\mathrm{j}\phi}\mathbf{C}_\mathrm{c}\mathbf{e}(k)\right\} \\ \tilde{\vartheta}(k+1) = \tilde{\vartheta}_\mathrm{g}(k) + T_\mathrm{s}\tilde{\omega}_\mathrm{g}(k) \end{cases} \tag{27}$$

where x_ω is an auxiliary state, and

$$\tilde{\omega}_\mathrm{g}(k) = -\frac{k_{\mathrm{p},\omega}}{u_{\mathrm{g}0}}\,\mathrm{Im}\left\{\frac{a}{b}\mathrm{e}^{\mathrm{j}\phi}\mathbf{C}_\mathrm{c}\mathbf{e}(k)\right\} - k_{\mathrm{i},\omega}x_\omega(k) \tag{28}$$

The system is linear and its numerical analysis becomes straightforward, if the complex space vectors are written in component form.

The closed-loop stability of the entire observer is examined when the design parameters of the observer are altered. The nominal system parameters are given in Table I. Stability is analyzed numerically by calculating eigenvalues of the linearized system (27). Fig. 6 illustrates stability regions of the closed-loop adaptive observer in the case of the different sampling periods $T_\mathrm{s} = 83.3$ μH and $T_\mathrm{s} = 125$ μH (corresponding the switching frequencies of 6 kHz and 4 kHz when two samples per period are obtained). Moreover, the regions where the damping ratios of the all eigenvalues are at least 0.2 and 0.7 are illustrated. The figure shows that the eigenvalues are well damped if the tuning parameters of the adaptation loops α_u and ω_ω are selected a decade down from α_od and ω_or.

[1]For stability analysis, $\tilde{u}_\mathrm{g}(k) = u_\mathrm{g}(k) - \hat{u}_\mathrm{g}(k)$, where u_g as an external disturbance can be set to zero.

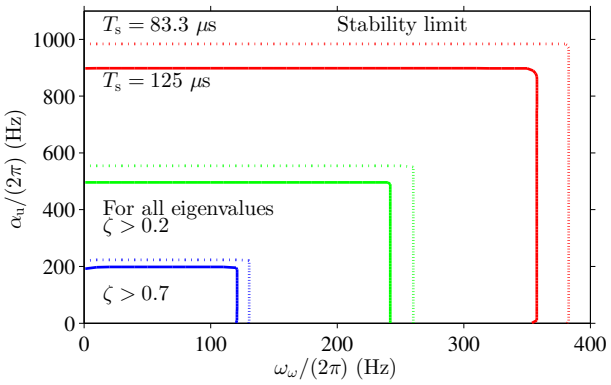

Fig. 6. Stability limits (red lines) of the adaptive observer as a function of the tuning parameters α_u and ω_ω when the other tuning parameters are: $\alpha_\mathrm{od} = 2\pi \cdot 1200$ rad/s, $\omega_\mathrm{or} = \omega_\mathrm{p}$, $\zeta_\mathrm{or} = 0.7$, and $\zeta_\omega = 1$. Two sampling periods are considered: $T_\mathrm{s} = 125$ μs (solid lines) and $T_\mathrm{s} = 83.3$ μs (dotted lines). Under the green lines, the damping ratios of the all eigenvalues are at least 0.2. Under the blue lines, the damping ratios are at least 0.7.

TABLE I
NOMINAL SYSTEM PARAMETERS

Param.	Value	Param.	Value
u_g	$\sqrt{2/3} \cdot 400$ V (1 p.u.)	L_fc	2.94 mH (0.072 p.u.)
ω_g	$2\pi \cdot 50$ rad/s	L_fg	1.96 mH (0.048 p.u.)
i_N	$\sqrt{2} \cdot 18$ A (1 p.u.)	C_f	10 μF (0.040 p.u.)
u_dc	650 V (2 p.u.)	ω_p	$2\pi \cdot 1470$ rad/s
f_sw	4 kHz	T_s	$1/(2f_\mathrm{sw}) = 125$ μs

IV. COMPARISON BETWEEN THE PROPOSED METHOD AND ITS CONTINUOUS-TIME COUNTERPART

An alternative for the proposed direct discrete-time design method is the continuous-time design method with an approximate discretization for digital implementation [11]. In comparison with the direct discrete-time design, continuous-time design is often easier and the models, e.g., system matrices, are simpler. However, the complexity of the continuous design is hidden in the digital implementation. For the full-order observer, Tustin's method for the discretization is needed in [11], which makes updating and computing the discrete approximation of the continuous-time observer at least as time-consuming as updating the proposed observer.

In order to compare the proposed observer and its continuous-time counterpart [11], the both observer designs were first simulated in the case of the nominal system parameters, cf. Table I. Fig. 7(a) shows the simulated responses of the estimation error when the converter current $\boldsymbol{i}_\mathrm{c}^\mathrm{g}$ (in the actual grid-voltage coordinates) was stepwise changed from $i_\mathrm{cd}^\mathrm{g} = 1.5$ p.u. to $i_\mathrm{cd}^\mathrm{g} = -1.5$ p.u. The both observers operate as designed and the steady-state errors are zero. The tuning parameters of the full-order observers correspond to Fig. 6: $\alpha_\mathrm{od} = 2\pi \cdot 1200$ rad/s, $\omega_\mathrm{or} = \omega_\mathrm{p}$ (ω_p is the resonance frequency of the LCL filter), $\zeta_\mathrm{or} = 0.7$. The tuning parameters for the adaptation loops were: $\alpha_\mathrm{u} = 2\pi \cdot 100$ rad/s, $\omega_\omega = 2\pi \cdot 50$ rad/s, and $\zeta_\omega = 1$. All the tuning parameters, including the sampling time $T_\mathrm{s} = 125$ μs, were the same for the both

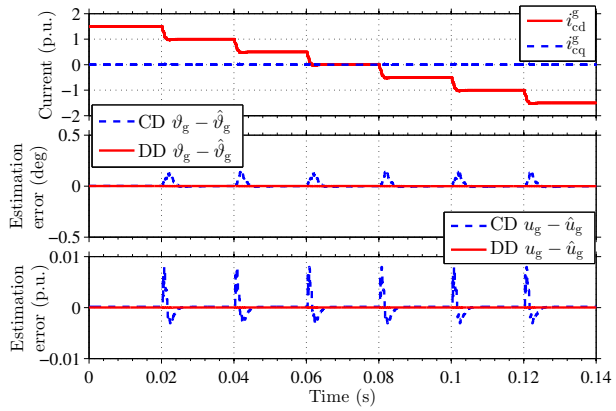

(a)

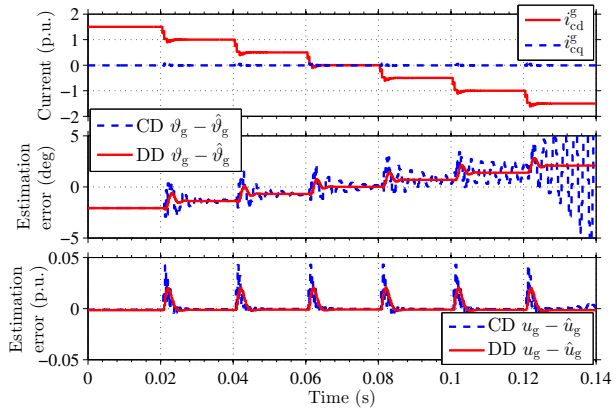

(b)

Fig. 7. Simulated estimation-error responses of the proposed observer (DD) and its continuous-time counterpart (CD, dashed line) when the operating point is changing: (a) the system parameters are nominal, and the sampling time of the both observers is $T_{\mathrm{s}} = 125$ μs; (b) the model parameters of the observers are erroneous (true L_{fg} is 50% larger than the nominal L_{fg} used in the observers), the sampling time is $T_{\mathrm{s}} = 250$ μs and the tuning parameter ω_ω is increased to $2\pi \cdot 150$ rad/s. Note that the scales of the y-axes of the figures (a) and (b) are not equal.

observers under comparison.

Fig. 7(b) shows the estimation-error responses in the case of the erroneous parameters and longer sampling time. For the both observers under comparison, the sampling time was doubled to $T_{\mathrm{s}} = 250$ μs which corresponds the switching frequency of 4 kHz with once-per-carrier synchronous sampling. The tuning parameter of the angle estimator was increased to $\omega_\omega = 2\pi \cdot 150$ rad/s for faster tracking of the grid-voltage angle. Moreover, the model parameters of the both observers were erroneous: the real grid-side inductance L_{fg} was increased by 50 % while the model parameters used by the observers were nominal. As the figure shows, the observer [11] that is designed in the continuous-time domain (blue dashed line) becomes unstable whereas the proposed observer (red solid line) is fully operational. Steady-state estimation errors depends on the operating-point. The results indicate that the proposed direct digital design is suitable for lower sampling frequencies than the continuous-time design [11]. Naturally, when the sampling frequency is higher, the functional difference between the compared methods is smaller.

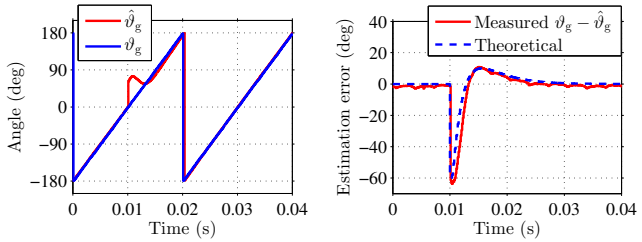

(a) (b)

Fig. 8. Experimental results when the disturbance impulse of $+60$ degrees is applied into the estimated grid-voltage angle: (a) estimated and actual angles; (b) measured angle-estimation error and corresponding theoretical response from (27).

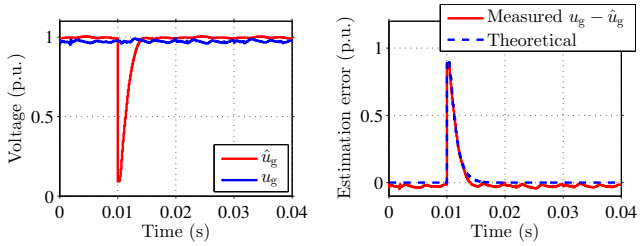

(a) (b)

Fig. 9. Experimental results when the disturbance impulse of -0.9 p.u. is applied into the estimated grid-voltage magnitude: (a) estimated and actual magnitudes; (b) measured magnitude-estimation error and corresponding theoretical response from (27).

V. Experimental Results

A. Validation

The proposed adaptive observer was experimentally tested as a part of grid-voltage sensorless control scheme shown in Fig. 1(b). The switching frequency of the 12.5-kVA, 400-V converter under test was 4 kHz and synchronous sampling (twice-per carrier) was used. The converter was connected to the electric power distribution system via a 1-MVA 20-kV/400-V transformer. The nominal system parameters are given in Table I. State-space current control [15], designed in the discrete-time domain, was used and the control algorithm was implemented on dSPACE DS1006 processor board. The converter under test was regulating the dc-bus voltage whereas another back-to-back connected converter was feeding power to the bus.

The current controller was tuned to give an approximate closed-loop bandwidth of 600 Hz. The dominant estimation-error dynamics were set twice as fast as the current-control bandwidth, i.e, $\alpha_{\mathrm{od}} = 2\pi{\cdot}1200$ rad/s and the second-order pole ω_{or} was set to the resonance frequency ω_{p} with the damping ratio of $\zeta_{\mathrm{or}} = 0.7$. The tuning parameters for the adaptation loops were: $\alpha_{\mathrm{u}} = 2\pi \cdot 100$ rad/s, $\omega_\omega = 2\pi \cdot 50$ rad/s, and $\zeta_\omega = 1$.

Fig. 8(a) shows the responses of the estimated and actual grid-voltage angles when the impulse disturbance of $+60^\circ$ was applied into the estimated angle $\hat{\vartheta}_{\mathrm{g}}$. At the same time, the

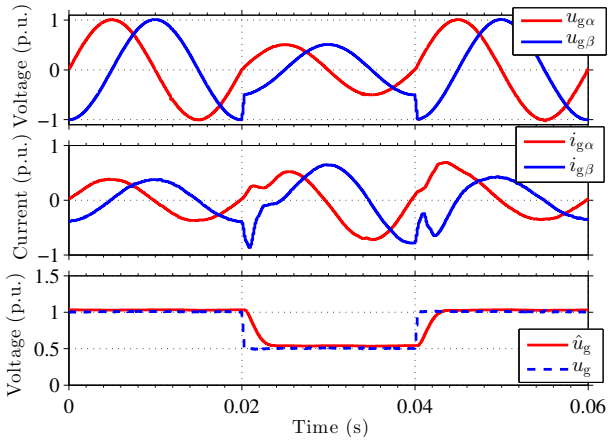

Fig. 10. Measured space-vector components $u_{g\alpha}$ and $u_{g\beta}$ of the grid voltage (above), the space-vector components i_α and i_β of the grid current (middle), and the estimated and actual grid-voltage magnitudes (below), when a grid-voltage dip is applied.

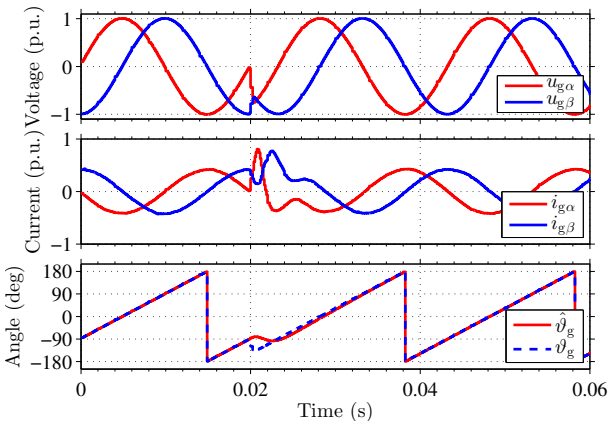

Fig. 11. Measured space-vector components $u_{g\alpha}$ and $u_{g\beta}$ of the grid voltage (above), the space-vector components i_α and i_β of the grid current (middle), and the estimated and actual grid-voltage angles (below), when a grid-voltage angle is changing rapidly $-60°$.

converter was supplying the power of 0.4 p.u. to the grid. Fig. 8(b) compares the measured angle-estimation error with the corresponding theoretical estimation error that is obtained from (27). As can be seen from the figure, the agreement between theoretical and measured estimation error is good. Moreover, the designed dynamic behavior is realized, cf. Fig. 5(b). The small 300-Hz ripple in the measured estimation error originates from the grid-voltage harmonics.

Fig. 9(a) shows the responses of the estimated and actual grid-voltage magnitudes when the impulse disturbance of -0.9 p.u. was applied into the estimated magnitude $\hat{u}_g$. At the same time, the converter was supplying the power of 0.4 p.u. to the grid. Fig. 9(b) compares the measured waveform of the magnitude-estimation error with the theoretical estimation error that is obtained from (27). As the figure shows, the agreement between the theoretical response and measurement is good. Furthermore, the measured estimation-error dynamics correspond the designed dynamics, cf. Fig. 5(a).

B. Operation Under Grid Disturbances

Operation of the grid-voltage sensorless control scheme was tested under grid-voltage dips and phase-angle jumps. The disturbances were supplied using a 50-kVA three-phase four-quadrant power supply (Regatron TopCon TC.ACS).

1) Grid Voltage Dip: Operation under a grid-voltage dip of 0.5 p.u. was evaluated. The converter was supplying the power of 0.4 p.u. to the grid. The measured responses of the estimated grid-voltage magnitude and the grid-current components i_α and i_β are shown in Fig. 10. As the figure shows, the estimated magnitude $\hat{u}_g$ rapidly follows the actual magnitude. The steady-state estimation error is small (0.03 p.u.) and it is explained by parameter uncertainties of the experimental setup.

2) Phase-Angle Jump: When the converter was rectifying the power of -0.4 p.u. from the grid, the grid-voltage angle was rapidly changed $-60°$. Fig. 11 shows the measured responses of the grid-current components i_α and i_β and the estimated and actual grid-voltage angles under the phase-angle jump. The steady-state estimation error of the angle is small ($0.5°$). As the figure shows, the estimated angle rapidly follows the actual angle and the steady-state operation is achieved in a half cycle of the grid voltage.

VI. Conclusion

This paper presents a discrete-time adaptive full-order observer for grid-voltage sensorless control of a grid-connected converter equipped with an LCL filter. The proposed analytical design method gives simple expressions for the gains of the observer scheme. The implementation of the method is straightforward following directly the digital design. According to the simulations, the proposed method is suitable for lower sampling rates than its continuous-time counterpart. Experimental results confirm the design method and indicate fast tracking of the grid-voltage amplitude and angle. Replacing the grid-voltage sensors with estimation provides cost savings. The proposed design could be applied, e.g., in active-front-end rectifiers of motor drives.

Appendix A
Parameters of the Discretized System

The state-transition matrix $\mathbf{\Phi} = \mathrm{e}^{\mathbf{A}T_\mathrm{s}}$ in (4) is

$$\mathbf{\Phi} = \gamma \begin{bmatrix} \frac{L_\mathrm{fc}+L_\mathrm{fg}\cos(\omega_\mathrm{p}T_\mathrm{s})}{L_\mathrm{t}} & -\frac{\sin(\omega_\mathrm{p}T_\mathrm{s})}{\omega_\mathrm{p}L_\mathrm{fc}} & \frac{L_\mathrm{fg}[1-\cos(\omega_\mathrm{p}T_\mathrm{s})]}{L_\mathrm{t}} \\ \frac{\sin(\omega_\mathrm{p}T_\mathrm{s})}{\omega_\mathrm{p}C_\mathrm{f}} & \cos(\omega_\mathrm{p}T_\mathrm{s}) & -\frac{\sin(\omega_\mathrm{p}T_\mathrm{s})}{\omega_\mathrm{p}C_\mathrm{f}} \\ \frac{L_\mathrm{fc}[1-\cos(\omega_\mathrm{p}T_\mathrm{s})]}{L_\mathrm{t}} & \frac{\sin(\omega_\mathrm{p}T_\mathrm{s})}{\omega_\mathrm{p}L_\mathrm{fg}} & \frac{[L_\mathrm{fg}+L_\mathrm{fc}\cos(\omega_\mathrm{p}T_\mathrm{s})]}{L_\mathrm{t}} \end{bmatrix} \tag{29}$$

where $\gamma = \mathrm{e}^{-\mathrm{j}\omega_\mathrm{g}T_\mathrm{s}}$, $L_\mathrm{t} = L_\mathrm{fc} + L_\mathrm{fg}$ and ω_p is the resonance frequency (3) of the LCL filter. The input vector for the converter voltage in (4) is

$$\mathbf{\Gamma}_\mathrm{c} = \gamma \begin{bmatrix} \frac{T_\mathrm{s}}{L_\mathrm{t}} + \frac{L_\mathrm{fg}\sin(\omega_\mathrm{p}T_\mathrm{s})}{\omega_\mathrm{p}L_\mathrm{fc}L_\mathrm{t}} \\ \frac{L_\mathrm{fg}[1-\cos(\omega_\mathrm{p}T_\mathrm{s})]}{L_\mathrm{t}} \\ \frac{T_\mathrm{s}}{L_\mathrm{t}} - \frac{\sin(\omega_\mathrm{p}T_\mathrm{s})}{\omega_\mathrm{p}L_\mathrm{t}} \end{bmatrix} \tag{30}$$

The elements of the input vector for the grid voltage $\boldsymbol{\Gamma}_\mathrm{g} = [\boldsymbol{b}_{\mathrm{g}1}\ \boldsymbol{b}_{\mathrm{g}2}\ \boldsymbol{b}_{\mathrm{g}3}]^\mathrm{T}$ in (4) are

$$\begin{aligned}
\boldsymbol{b}_{\mathrm{g}1} &= \frac{\boldsymbol{\gamma}\left[-\omega_\mathrm{g}\omega_\mathrm{p}\sin(\omega_\mathrm{p}T_\mathrm{s}) + \mathrm{j}\omega_\mathrm{g}^2\cos(\omega_\mathrm{p}T_\mathrm{s}) - \mathrm{j}\rho\right] - \mathrm{j}\omega_\mathrm{p}^2}{\rho\omega_\mathrm{g}(L_\mathrm{fc}+L_\mathrm{fg})} \\
\boldsymbol{b}_{\mathrm{g}2} &= \frac{\boldsymbol{\gamma}\left[\omega_\mathrm{p}\cos(\omega_\mathrm{p}T_\mathrm{s}) + \mathrm{j}\omega_\mathrm{g}\sin(\omega_\mathrm{p}T_\mathrm{s})\right] - \omega_\mathrm{p}}{\rho\omega_\mathrm{p}C_\mathrm{f}L_\mathrm{fg}} \\
\boldsymbol{b}_{\mathrm{g}3} &= \boldsymbol{\gamma}\frac{\omega_\mathrm{g}\omega_\mathrm{p}L_\mathrm{fc}\sin(\omega_\mathrm{p}T_\mathrm{s}) - \mathrm{j}\rho L_\mathrm{fg} - \mathrm{j}\omega_\mathrm{g}^2 L_\mathrm{fc}\cos(\omega_\mathrm{p}T_\mathrm{s})}{\rho\omega_\mathrm{g}L_\mathrm{fg}(L_\mathrm{fc}+L_\mathrm{fg})} \\
&\quad + \frac{\mathrm{j}\rho L_\mathrm{fg} + \mathrm{j}\omega_\mathrm{g}^2 L_\mathrm{fc}}{\rho\omega_\mathrm{g}L_\mathrm{fg}(L_\mathrm{fc}+L_\mathrm{fg})},
\end{aligned} \tag{31}$$

where $\rho = \omega_\mathrm{g}^2 - \omega_\mathrm{p}^2$.

Appendix B
Small-Signal Linearization of the Estimation-Error Dynamics

When the stable operation of the observer is assumed, the nonlinear estimation-error dynamics (11)

$$\mathbf{e}(k+1) = \boldsymbol{f}[\mathbf{e}(k), \mathbf{x}(k), \boldsymbol{u}_\mathrm{c}(k), u_\mathrm{g}(k), \tilde{u}_\mathrm{g}(k), \tilde{\vartheta}(k), \tilde{\omega}(k)] \tag{32}$$

have an equilibrium point (marked with the subscript 0)

$$\mathbf{e}_0 = \boldsymbol{f}[\mathbf{e}_0, \mathbf{x}_0, \boldsymbol{u}_{\mathrm{c}0}, u_{\mathrm{g}0}, \tilde{u}_{\mathrm{g}0}, \tilde{\vartheta}_0, \tilde{\omega}_0] \tag{33}$$

If the circuit parameters are accurate ($\hat{L}_\mathrm{fg} = L_\mathrm{fc}$, $\hat{C}_\mathrm{f} = C_\mathrm{f}, \hat{L}_\mathrm{fg} = L_\mathrm{fg}$) in the observer matrices and the frequency estimation error is zero ($\tilde{\omega}_0 = \omega_{\mathrm{g}0} - \hat{\omega}_{\mathrm{g}0} = 0$), the system matrices are equal $\hat{\boldsymbol{\Phi}}_0 = \boldsymbol{\Phi}_0$, $\hat{\boldsymbol{\Gamma}}_{\mathrm{c}0} = \boldsymbol{\Gamma}_{\mathrm{c}0}$, and $\hat{\boldsymbol{\Gamma}}_{\mathrm{g}0} = \boldsymbol{\Gamma}_{\mathrm{g}0}$. It follows that the estimation errors are zero $\{\mathbf{e}_0 = 0,\ \tilde{u}_{\mathrm{g}0} = 0,\ \tilde{\omega}_0 = 0,\ \tilde{\vartheta}_0 = 0\}$ at the equilibrium point with the accurate parameters. In the vicinity of the equilibrium, the small-signal deviation is marked with δ, e.g., $\delta\tilde{\vartheta} = \tilde{\vartheta} - \tilde{\vartheta}_0$. In terms of the small-signal deviations, the estimation error dynamics around the equilibrium are

$$\begin{aligned}
\delta\mathbf{e}(k+1) &= \left(\frac{\partial \boldsymbol{f}}{\partial \mathbf{e}}\right)_0 \delta\mathbf{e}(k) + \left(\frac{\partial \boldsymbol{f}}{\partial \mathbf{x}}\right)_0 \delta\mathbf{x}(k) \\
&\quad + \left(\frac{\partial \boldsymbol{f}}{\partial \boldsymbol{u}_\mathrm{c}}\right)_0 \delta\boldsymbol{u}_\mathrm{c}(k) + \left(\frac{\partial \boldsymbol{f}}{\partial u_\mathrm{g}}\right)_0 \delta u_\mathrm{g}(k) \\
&\quad + \left(\frac{\partial \boldsymbol{f}}{\partial \tilde{u}_\mathrm{g}}\right)_0 \delta\tilde{u}_\mathrm{g}(k) + \left(\frac{\partial \boldsymbol{f}}{\partial \tilde{\vartheta}}\right)_0 \delta\tilde{\vartheta}(k) \\
&\quad + \left(\frac{\partial \boldsymbol{f}}{\partial \tilde{\omega}}\right)_0 \delta\tilde{\omega}(k)
\end{aligned} \tag{34}$$

when constant ω_g is assumed, i.e., $\delta\omega_\mathrm{g} = 0$. All the partial derivatives are evaluated at the equilibrium point, and they are

$$\begin{aligned}
\left(\frac{\partial \boldsymbol{f}}{\partial \mathbf{e}}\right)_0 &= \boldsymbol{\Phi}_0 - \mathbf{K}_\mathrm{o}\mathbf{C}_\mathrm{c} \\
\left(\frac{\partial \boldsymbol{f}}{\partial \mathbf{x}}\right)_0 &= \left(\frac{\partial \boldsymbol{f}}{\partial \boldsymbol{u}_\mathrm{c}}\right)_0 = \left(\frac{\partial \boldsymbol{f}}{\partial u_\mathrm{g}}\right)_0 = 0 \\
\left(\frac{\partial \boldsymbol{f}}{\partial \tilde{u}_\mathrm{g}}\right)_0 &= \boldsymbol{\Gamma}_{\mathrm{g}0}, \qquad \left(\frac{\partial \boldsymbol{f}}{\partial \tilde{\vartheta}}\right)_0 = \mathrm{j}u_{\mathrm{g}0}\boldsymbol{\Gamma}_{\mathrm{g}0} \\
\left(\frac{\partial \boldsymbol{f}}{\partial \tilde{\omega}}\right)_0 &= \left[\mathrm{j}\boldsymbol{\Gamma}_{\mathrm{g}0}T_\mathrm{s} - \left(\frac{\mathrm{d}\hat{\boldsymbol{\Gamma}}_\mathrm{g}}{\mathrm{d}\tilde{\omega}}\right)_0\right] u_{\mathrm{g}0}
\end{aligned} \tag{35}$$

It is to be noted that the system matrices of the observer $\hat{\boldsymbol{\Phi}}$, $\hat{\boldsymbol{\Gamma}}_\mathrm{c}$, and $\hat{\boldsymbol{\Gamma}}_\mathrm{g}$ are similar to $\boldsymbol{\Phi}$, $\boldsymbol{\Gamma}_\mathrm{c}$, and $\boldsymbol{\Gamma}_\mathrm{g}$, but instead of ω_g, they are functions of $\hat{\omega}_\mathrm{g}$. Thus, they are functions of $\tilde{\omega} = \omega_\mathrm{g} - \hat{\omega}_\mathrm{g}$ and their partial derivatives are considered with respect to $\tilde{\omega}$ in (35). In order to shorten notation, δ is left out in the resulting linearized dynamics (12) and in Section III.

Acknowledgment

The authors would like to thank ABB Oy, Finnish Foundation for Technology Promotion, and the Emil Aaltonen Foundation for the financial support.

References

[1] *IEEE Standard for Interconnecting Distributed Resources with Electric Power Systems*, IEEE Std. 1547-2003, Jul. 2003.

[2] K. Jalili and S. Bernet, "Design of LCL filters of active-front-end two-level voltage-source converters," *IEEE Trans. Ind. Electron.*, vol. 56, no. 5, pp. 1674–1689, May 2009.

[3] F. Betin, G.-A. Capolino, D. Casadei, B. Kawkabani, R. I. Bojoi, L. Harnefors, E. Levi, L. Parsa, and B. Fahimi, "Trends in electrical machines control: Samples for classical, sensorless, and fault-tolerant techniques," *IEEE Ind. Electron. Mag.*, vol. 8, no. 2, pp. 43–55, Jun. 2014.

[4] M. Malinowski and S. Bernet, "A simple voltage sensorless active damping scheme for three-phase PWM converters with an LCL filter," *IEEE Trans. Ind. Electron.*, vol. 55, no. 4, pp. 1876–1880, Apr. 2008.

[5] J. A. Suul, A. Luna, P. Rodriguez, and T. Undeland, "Voltage-sensor-less synchronization to unbalanced grids by frequency-adaptive virtual flux estimation," *IEEE Trans. Ind. Electron.*, vol. 59, no. 7, pp. 2910–2923, Jul. 2012.

[6] G. Wrona and K. Malon, "Sensorless operation of an active front end converter with LCL filter," in *Proc. ISIE 2014*, Istanbul, Turkey, Jun. 2014, pp. 2697–2702.

[7] B. Bolsens, K. De Brabandere, J. Van den Keybus, J. Driesen, and R. Belmans, "Model-based generation of low distortion currents in grid-coupled PWM-inverters using an LCL output filter," *IEEE Trans. Power Electron.*, vol. 21, no. 4, pp. 1032–1040, Jul. 2006.

[8] K. H. Ahmed, A. M. Massoud, S. J. Finney, and B. W. Williams, "Sensorless current control of three-phase inverter-based distributed generation," *IEEE Trans. Power Del.*, vol. 24, no. 2, pp. 919–929, Apr. 2009.

[9] S. Mariéthoz and M. Morari, "Explicit model-predictive control of a PWM inverter with an LCL filter," *IEEE Trans. Ind. Electron.*, vol. 56, no. 2, pp. 389–399, Feb. 2009.

[10] Y. A.-R. I. Mohamed, M. A.-Rahman, and R. Seethapathy, "Robust line-voltage sensorless control and synchronization of LCL-filtered distributed generation inverters for high power quality grid connection," *IEEE Trans. Power Electron.*, vol. 27, no. 1, pp. 87–98, Jan. 2012.

[11] J. Kukkola and M. Hinkkanen, "State observer for grid-voltage sensorless control of a grid-connected converter equipped with an LCL filter," in *Proc. EPE'14-ECCE Europe*, Lappeenranta, Finland, Aug. 2014.

[12] D.-C. Lee and D.-S. Lim, "AC voltage and current sensorless control of three-phase PWM rectifiers," *IEEE Trans. Power Electron.*, vol. 17, no. 6, pp. 883–890, Nov. 2002.

[13] V. Miskovic, V. Blasko, T. M. Jahns, R. D. Lorenz, C. J. Romenesko, and H. Zhang, "Synchronous frame and resonant adaptive observers as disturbance estimators and their applications in power electronics," in *Proc. IEEE ECCE 2014*, Pittsburgh, PA, Sep. 2014, pp. 1248–1255.

[14] T. Tuovinen, M. Hinkkanen, L. Harnefors, and J. Luomi, "Comparison of a reduced-order observer and a full-order observer for sensorless synchronous motor drives," *IEEE Trans. Ind. Appl.*, vol. 48, no. 6, pp. 1959–1967, Nov. 2012.

[15] J. Kukkola, M. Hinkkanen, and K. Zenger, "Observer-based state-space current controller for a grid converter equipped with an LCL filter: Analytical method for direct discrete-time design," *IEEE Trans. Ind. Appl.*, vol. 51, no. 5, pp. 4079–4090, Sep./Oct. 2015.